ARTICLE

Reconfigurable soft body trajectories using unidirectionally stretchable composite laminae

Sang Yup Kim [1,4], Robert Baines [1,4], Joran Booth[1], Nikolaos Vasios[2,3], Katia Bertoldi[2,3] & Rebecca Kramer-Bottiglio[1]

Compliant, continuum structures allow living creatures to perform complex tasks inaccessible to artificial rigid systems. Although advancements in hyper-elastic materials have spurred the development of synthetic soft structures (i.e., artificial muscles), these structures have yet to match the precise control and diversity of motions witnessed in living creatures. Cephalopods tentacles, for example, can undergo multiple trajectories using muscular hydrostat, a structure consisting of aggregated laminae of unidirectional muscle fibers. Here, we present a self-adhesive composite lamina inspired by the structural morphology of the muscular hydrostat, which adheres to any volumetrically expanding soft body to govern its motion trajectory. The composite lamina is stretchable only in one direction due to inextensible continuous fibers unidirectionally embedded within its hyper-elastic matrix. We showcase reconfiguration of inflation trajectories of two- and three-dimensional soft bodies by simply adhering laminae to their surfaces.

[1] School of Engineering and Applied Science, Yale University, New Haven, CT 06511, USA. [2] Harvard John A. Paulson School of Engineering and Applied Sciences, Harvard University, Cambridge, MA 02138, USA. [3] Kalvi Institute of Bionano Science & Technology, Harvard University, Cambridge, MA 02138, USA. [4] These authors contributed equally: Sang Yup Kim, Robert Baines. Correspondence and requests for materials should be addressed to R.K.-B. (email: rebecca.kramer@yale.edu)

The introduction and critical study of hyper-elastic materials have sparked an evolution in numerous domains of science and engineering, such as medicine[1,2], electronics[3–5], and robotics[6–8]. The inherent stretchability and resilience of hyperelastic materials make them apt for incorporation into devices imitating the physiology of living creatures. In robotics, hyperelastic materials allow for the creation of compliant, continuum soft robots with greater adaptability and flexibility than conventional linkage-joint robots[9–13]. Many soft robots inspired by the morphology of biological organisms have performed movements of unprecedented complexity. A typical mechanism to impart such sophisticated movement is the incorporation of strain limiters onto a soft body. When the body inflates, strain limiters exert contraction forces analogous to biological muscle fibers, governing specific shape changes[14–20]. McKibben and PneuNet actuators are pneumatic artificial muscles widely used in practice, and exploit confinement in woven mesh[21,22] or by rigid compartments, as strain limiters[23–25]. However, these actuators are often suboptimal for use in entirely-soft robots: McKibben actuators are difficult to integrate into soft bodies without rigid fixtures, and PneuNets are challenging to predict and control due to their intricate geometry. Recent studies have established a simple yet effective way to control the deformation trajectory of soft actuators—by wrapping them with continuous inextensible fibers[26–29]. Varying the angle of wrapped fibers creates unique strain-limiting patterns that change how an internal elastomeric bladder expands, and allows for predictable extension, twisting, and bending. However, in this approach, programmed directionality is permanent and constrained to one fixed motion, unlike the versatility exhibited by biological organisms. Additionally, fiber-wrapped actuators have tedious manufacturing processes that make them difficult to integrate with two-dimensional (2D) geometries or scale up.

Looking to nature for inspiration in addressing the aforementioned challenges with existing soft actuators, we noticed that remarkably dexterous motion achieved by skeleton-free animal parts such as elephant trunks, octopus arms, and human tongues, is attributed to muscular hydrostats: a laminated structure composed of layers of unidirectional muscle fibers[30]. Selective contraction of individual muscle layers in three primary axes—transverse, longitudinal, and oblique—grants muscular hydrostats the ability to move precisely and with infinite degrees of freedom[31,32]. For example, cephalopod tentacles twist by contracting oblique muscle fibers and bend by simultaneously contracting transverse and longitudinal muscle fibers (Fig. 1a). A simple superposition of these unidirectional muscle contraction primitives gives rise to sophisticated deformation.

Inspired by the fiber architecture of the muscular hydrostat, we developed a lamina composed of a hyper-elastic matrix with unidirectionally embedded inextensible fibers and an adhesive backing (Fig. 1b). We call this composite material Stretchable Adhesive Uni-Directional prepreg (STAUD-prepreg). STAUD-prepreg is extremely stretchable in the direction perpendicular to the fibers and inextensible along the fibers, boasting a 1000-fold difference in stiffness and elongation (Fig. 1c). When STAUD-prepreg is adhered to volumetrically expanding soft bodies, the embedded inextensible fibers induce selective contraction forces analogous to muscle fibers in the muscular hydrostat, and govern shape change (Fig. 1d, Supplementary Movie 1). The fabrication of STAUD-prepreg is simple and scalable, leveraging a fiber-winding process that is already established in industry for mass-production of industrial-grade composites to create large 2D sheets, which can be cut and applied to almost any soft actuator. Namely, we use a bench-top fiber winder wherein a mixture of two-part silicone resin is infused into polyester fibers uniformly spaced on a rotating mandrel (Fig. 1e). We then apply a silicone-based adhesive to the back of the lamina after the resin fully cures to create a self-adhesive layer. The deformation trajectories of soft bodies are easy to program by placing STAUD-prepreg on their surfaces (Fig. 1f). Adhered STAUD-prepreg can be easily detached and re-attached in various patterns and stacking sequences to reconfigure the inflation trajectories.

Results

Influence of STAUD-prepreg on soft actuator trajectories. To reveal the influence of STAUD-prepreg on morphing trajectories of soft bodies, we began by constructing a freely-inflating cylindrical actuator wrapped in one STAUD-prepreg. By adjusting the fiber orientation of this STAUD-prepreg, the cylindrical actuator exhibits a variety of motions such as contraction, elongation, and rotation (Fig. 2a). Contraction (Fig. 2a at 0°, Supplementary Movie 2) is accomplished when the STAUD-prepreg is wrapped at $\theta = 0°$; that is, embedded fibers are aligned longitudinally to the cylinder length. The 0° fibers geometrically constrain the pneumatic cylinder such that it is only capable of expanding transversely, resulting in length-wise contraction. Elongation (Fig. 2a at 90°, Supplementary Movie 3) is achieved with the STAUD-prepreg fibers oriented at $\theta = 90°$; that is, embedded fibers are aligned perpendicular to the cylinder's length. The 90° fibers prevent the actuator from expanding transversely, forcing it to extend axially. Rotation (Fig. 2a at 45°, Supplementary Movie 4) occurs in a manner similar to elongation, except the angled fibers ($\theta = 45°$ in this study) exert a torque with respect to the central axis. In all cases, the deformation of a cylindrical actuator is proportional to the input pressure and directly affected by the fiber spacing of the adhered prepreg. Moreover, STAUD-prepreg are capable of programming inflation trajectories of 2D objects and controlling their shape in 3D space. For instance, applying STAUD-prepreg to a thin, planar soft body elicits bending upon its inflation (Fig. 2b, Supplementary Movie 5). Planar actuators outfitted with STAUD-prepreg are light and occupy a small footprint when not actuated, making them ideal for deployable, easily-transportable pneumatic devices. In general, the initial shape of soft bodies (i.e., 2D vs 3D cylinder) influences more the adherence of the STUAD-prepreg, than it does the uniqueness of a final shape. The 2D configuration of STAUD-prepreg is easier to adhere to 2D bodies than 3D ones without void entrapments that can potentially degrade the adhesion quality.

Mechanical characterization of STAUD-prepreg. We conducted tensile mechanical testing of STAUD-prepreg laminae with different fiber orientations and spacings to ascertain its fundamental mechanical properties. Quasi-static, unidirectional tensile tests reveal a stark difference in stretchability (i.e., stiffness and elongation) of the material, depending on the loading direction (Fig. 2c). For example, the tensile modulus of the lamina (at 2 mm fiber spacing) is 56 MPa in the longitudinal direction of the fibers (E_1), and 0.065 MPa in the transverse direction (E_2). Moduli tend to increase with decreasing fiber spacing as a result of the higher fiber content in the lamina[33]. Theoretically calculated values from micromechanics modeling[34] confirm our experimental results for moduli:

$$E_1 = V_f E_f + V_m E_m \tag{1}$$

$$E_2 = (V_f/E_f + V_m/E_m)^{-1} \tag{2}$$

where E_f and E_m are tensile moduli of fibers and matrix, and V_f and V_m are the volume fraction of fibers and matrix, respectively (see "Supplementary method" for details).
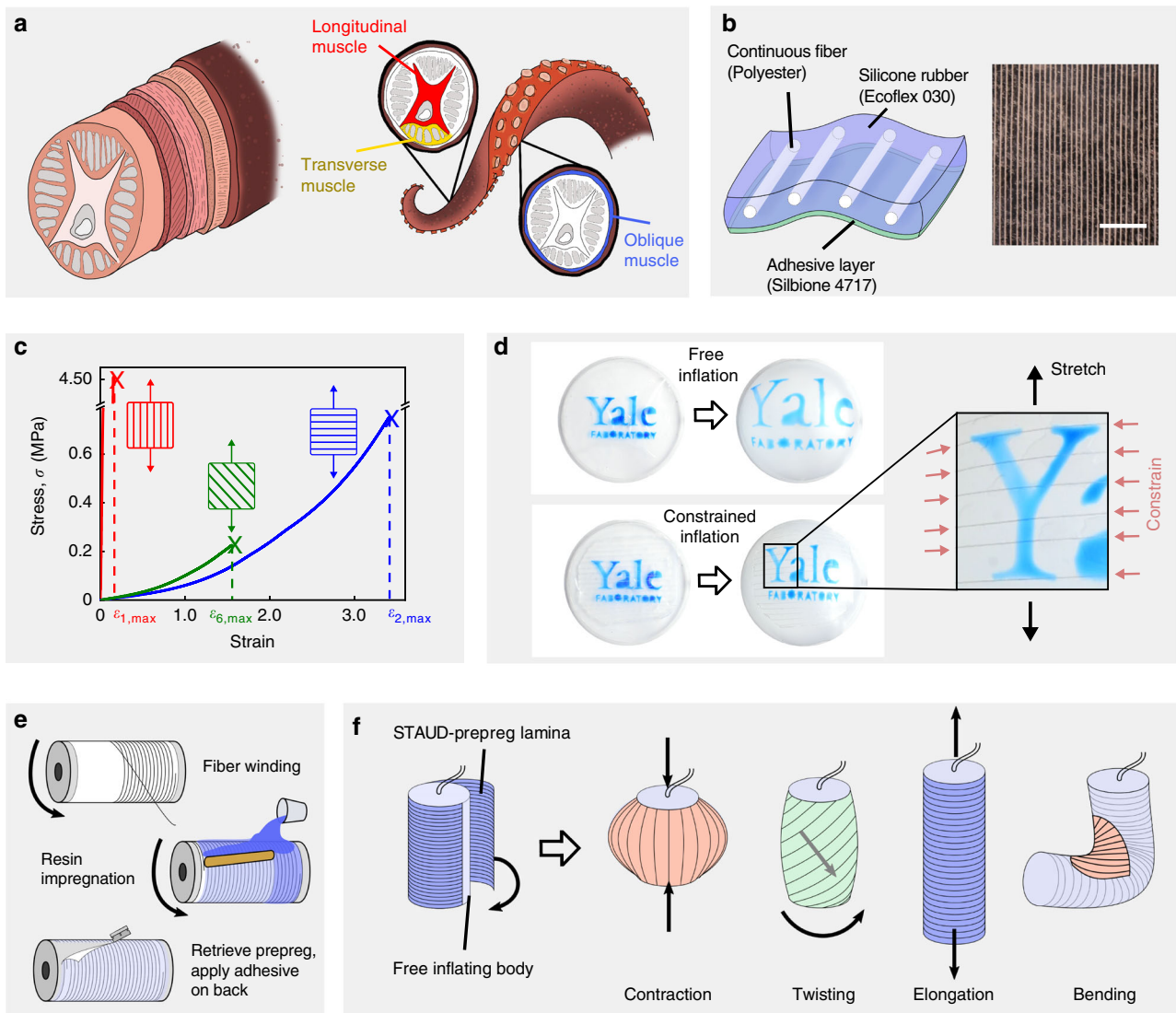
Fig. 1 Overview and working principle of STAUD-prepreg. **a** Illustration of laminated layers of unidirectional muscle fibers in a muscular hydrostat in cephalopod tentacles and the working mechanism for achieving complex motion. **b** Schematic and optical micrograph of stretchable adhesive unidirectional prepreg (STAUD-prepreg). Scale bar: 10 mm. **c** Quasi-static uniaxial tensile testing results of STAUD-prepreg laminae with respect to different fiber orientations ($\theta = 0°$, 45°, 90° from left). **d** Photographs of inflating planar soft body. Free inflation (top) with uniform radial expansion and constrained inflation (bottom) with one adhered lamina at $\theta = 90°$. **e** Schematic of fabrication process for STAUD-prepreg using a bench-top fiber winder. **f** Illustration of cylindrical actuators with one STAUD-prepreg lamina adhered, and the ensuing inflation trajectory

Analytic prediction of deformation. To predict deformation of an inflating body outfitted with STAUD-prepreg, we used our experimental tensile test results to construct a stiffness matrix ($\mathbf{C}_{ij}$) of the lamina, for a relation $\sigma_i = \mathbf{C}_{ij}\varepsilon_{ij}$ ($i, j = 1, 2, 3, \ldots 6$), where $\boldsymbol{\sigma}$ is stress and $\boldsymbol{\varepsilon}$ is strain. Since STAUD-prepreg is thin and its properties are symmetric about one axis, the stiffness matrix is further simplified to $[\mathbf{Q}]_{x,y}$, for a relation $[\boldsymbol{\sigma}]_{x,y} = [\mathbf{Q}]_{x,y}[\boldsymbol{\varepsilon}]_{x,y}$, where $[\boldsymbol{\sigma}]_{x,y}$ and $[\boldsymbol{\varepsilon}]_{x,y}$ are stress and strain matrices in the x-y plane, respectively[35]. This stiffness matrix allows us to analytically predict morphing of the host body clad in STAUD-prepreg laminae, after a slight modification to classical laminate theory[36–38]:

$$\sum_{k=1}^{n}\int_{z_{k-1}}^{z_k}[\boldsymbol{\sigma}]_{x,y}^k \mathrm{d}z = \sum_{k=1}^{n}\int_{z_{k-1}}^{z_k}[\mathbf{Q}]_{x,y}^k[\boldsymbol{\varepsilon}]_{x,y}^k \mathrm{d}z \qquad (3)$$

where k is an individual lamina, n is the total number of laminae, and z is the out-of-plane coordinate (see "Supplementary

method" for details). A prediction model from the augmented classical laminate theory (ACLT) shows good agreement with the experimental strain values of the cylindrical actuators in Fig. 2a, using Eq. (3) at $n = 1$. Adapting ACLT to the soft robotics space facilitates the prediction of the morphing of soft bodies clad in STAUD-prepreg, and enables intuitive programming of specific motions.

Influence of multiple STAUD-prepreg on soft actuator trajectories. To impart more complex motion on a soft body, we created actuators with STAUD-prepreg patterns emulating the muscular hydrostat structure. For instance, we adhered multiple STAUD-prepreg in a stack, or cut a single STAUD-prepreg into various-sized patches, and distributed them across a soft body's surface. We used a cylindrical actuator in Fig. 2a at 90° as a base that forced elongation, and adhered additional STAUD-prepreg to further direct motion. When a STAUD-prepreg with $\theta = 0°$ was adhered in a way that covered the entire base, the actuator
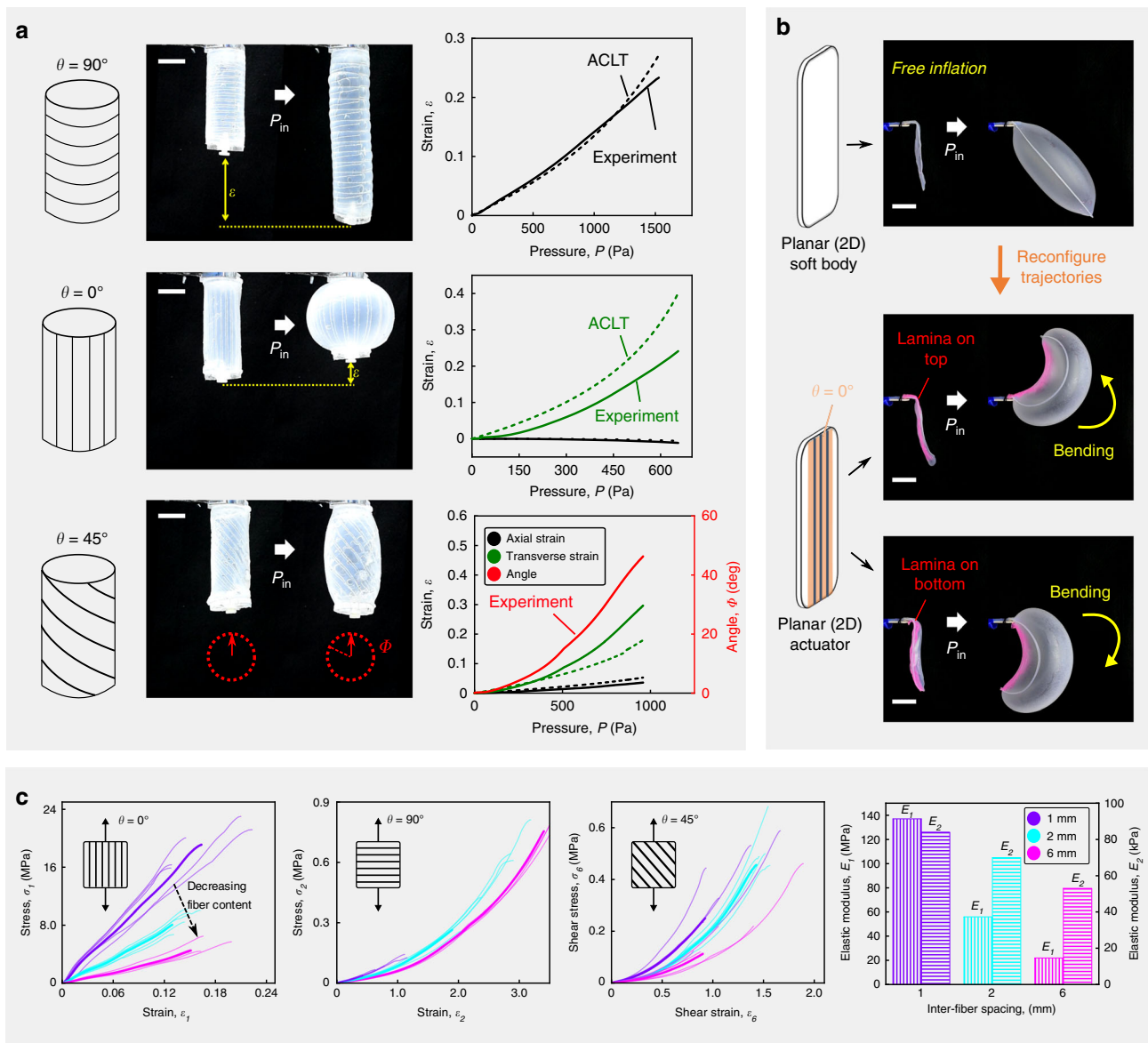
Fig. 2 Basic programmed inflation trajectory of 2D/3D soft bodies and mechanical characterization of STAUD-prepreg. **a** Inflating cylindrical actuator wrapped with one STAUD-prepreg lamina at different fiber orientations of $\theta = 90°$, $0°$ and $45°$. Experimental results are juxtaposed with analytical results from augmented classical laminate theory (ACLT). Legend color codes apply to all plots. Scale bar: 25 mm. **b** Planar soft body consisting of two silicone rubber films and reconfiguration of its inflation trajectory by adhering one STAUD-prepreg. Scale bar: 25 mm. **c** Quasi-static uniaxial tensile testing results for STAUD-prepreg. E_1 and E_2 denote the Young's modulus of the STAUD-prepreg along the fibers ($\theta = 0°$) and perpendicular to the fibers ($\theta = 90°$), respectively. Higher fiber content in the prepreg results in lager values of E_1 and E_2. E_1 is ~1000-times greater than E_2

underwent virtually no motion due to the presence of strain-limiting fibers preventing extension in both principal directions (Fig. 3a). Replacing the adhered STAUD-prepreg ($\theta = 0°$) with one at $\theta = 45°$ gave rise to rotational motion with a negligible expansion in volume, unlike the actuator with one lamina adhered at $\theta = 45°$ (see Fig. 2a at 45°). The ACLT model at $n = 2$ in Eq. (3) shows good agreement with experimental results and confirms the utility of ACLT in predicting the deformation of actuators clad in STAUD-prepreg. When a bulk STAUD-prepreg is cut into patches and adhered to the elongating base actuator, we coerce deformations that cannot be attained with actuators whose surfaces are entirely covered by STAUD-prepreg (see Figs. 2a, 3a), and unlock a larger workspace without any significant jumps in mechanical complexity. For example, bending, the underlying motion for grasping and locomotion in cephalopods, is achieved in our system when one STAUD-prepreg patch

is adhered to locally confine elongation (Fig. 3b, Supplementary Movie 6). Adjusting the fiber orientation of the patch results in a compound bending and twisting motion (Fig. 3c). Further complex output motion arises when multiple STAUD-prepreg patches are attached to the actuator in different locations. Each adhered patch creates contraction forces on the actuator based on its respective dimensions (i.e., w and h) and elicits unique trajectories (Fig. 3d).

Numerical modeling of deformation. We performed finite element (FE) analysis on cylindrical actuators' motion using ABAQUS commercial software (see "Supplementary method" for details). FE simulation results confirm our experimental results and reveal detailed strain and stress fields on the inflating actuator (Fig. 3e as an example for the bending motion in
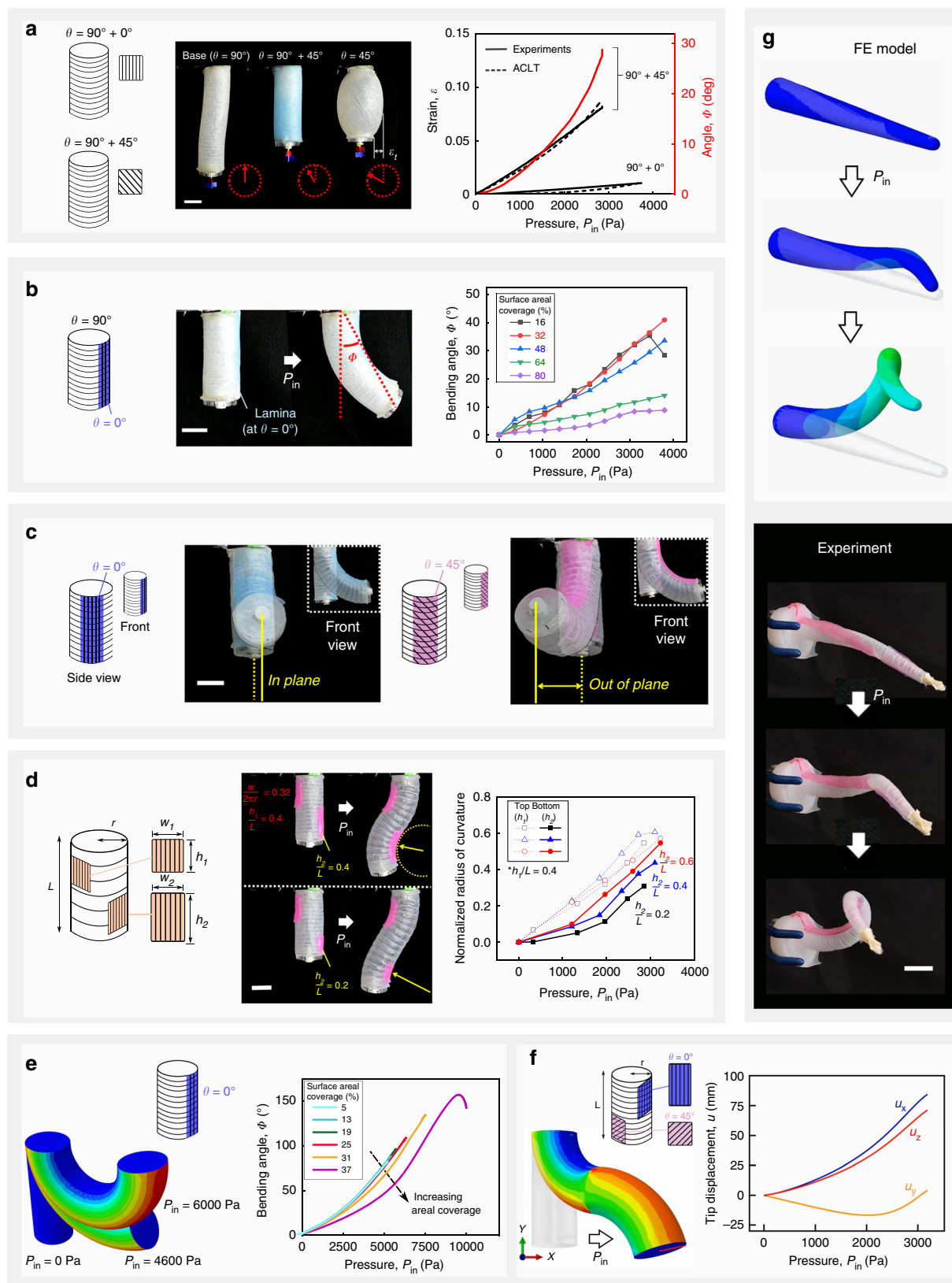
Fig. 3b). Moreover, FE modeling allows prediction of the influence of localized patch(es) on a soft body otherwise too complicated for ACLT to predict (Fig. 3f). We utilized the FE modeling to obtain STAUD-prepreg patch designs that when adhered to a slender soft body elicit dexterous movements similar to cephalopods tentacles. We then reproduced the simulated results in the laboratory (Fig. 3g, Supplementary Movie 7). Experimental results show good agreement with the simulation, testifying to the fact that FE modeling serves as an accurate design tool.

Fig. 3 Complex programmed inflation trajectory of 3D soft bodies and finite element simulation. **a** Elongating cylindrical actuator (at $\theta = 90°$) with an additional STAUD-prepreg wrapped around at $\theta = 0°$ or $45°$. The addition of a STAUD-prepreg at $\theta = 0°$ immobilizes the actuator, while one at $\theta = 45°$ gives rise to rotational motion without transverse strain (ε_t). Scale bar: 25 mm. **b**–**d** Bending motion of a cylindrical actuator due to a segmented STAUD-prepreg patch. **b** Increasing the areal coverage of the patch decreases the bending angle at a given pressure. **c** Adhering a patch at $\theta = 45°$ elicits a mixed motion of bending and twisting. **d** Two-localized patches with increasing patch dimension along the actuator length leads to a higher bending curvature. Scale bar: 25 mm. **e**, **f** Finite element (FE) analysis results using ABAQUS on cylindrical actuators. **e** Bending angle as a function of input pressure and a patch's areal coverage, as gathered from the simulation. **f** Two-localized patches with different fiber angles (at $\theta = 0°$ and $45°$). **g** A slender cylindrical actuator mimicking the motion of cephalopod tentacles. FE simulation of the actuator with particular patch pattern and dimensions matches with the experiment. Scale bar: 50 mm
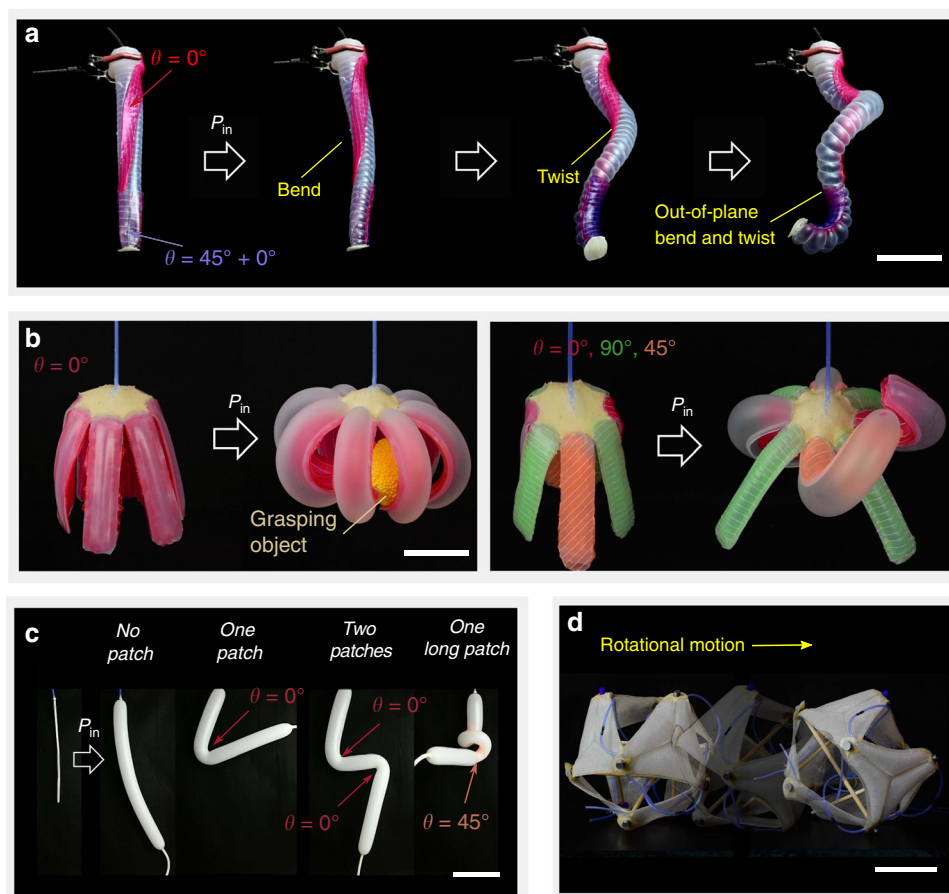
Fig. 4 Practical use cases for STAUD-prepreg controlling compliant systems. **a** Life-like complex grasping motion akin to cephalopod tentacles accomplished by a cylindrical actuator. Scale bar: 100 mm. **b** Planar soft body with eight tentacles for use as a pop-up gripper. Adhering STAUD-prepreg patches gives rise to specific movements of individual tentacles that previously inflated without directional bias. Scale bar: 50 mm. **c** Conventional balloon with adhered STAUD-prepreg patches. The fiber orientation and dimension of the applied patches determine the inflation trajectories of the balloon. Scale bar: 50 mm. **d** A tensegrity robot consisting of rigid struts and soft membrane actuators made from STAUD-prepreg. A combination of rigid components and soft, planar actuators allows this hybrid system to roll from face to face by inflating the membrane actuators to locally destabilize itself. Scale bar: 200 mm

Demonstrations using STAUD-prepreg. We demonstrated several practical use cases for STAUD-prepreg. First, linearly scaling up the dimensions of the actuator in Fig. 3d gives rise to a life-like grasping motion; a combined movement of wrapping and bending reminiscent of cephalopod tentacles (Fig. 4a, Supplementary Movie 7). We then created a planar actuator consisting of eight tentacles that inflate uniformly without directional bias. Attaching STAUD-prepreg patches of varying fiber orientation enabled us to individually control the tentacles' shapes during inflation (Fig. 4b, Supplementary Movie 8). The planar actuator outfitted with STAUD-prepreg is capable of grasping and twisting an object, although it is significantly lighter and more

compactable compared to conventional soft grippers. The versatility of STAUD-prepreg is further demonstrated by its application to every-day soft bodies, such as balloons (Fig. 4c, Supplementary Movie 9). When adhered to a balloon, STAUD-prepreg patches govern its inflation trajectory based on the quantity, dimensions, and fiber orientations of the patches. This reaffirms how balloons—cheap and ubiquitous as they are—could be used as programmable actuators in soft robots. Moreover, we made planar membrane actuators to change the shape of skeletal robotic systems. In particular, we created thin elastomer membranes outfitted with a layer of STAUD-prepreg to interface the compressive members of a tensegrity robot. The membrane

actuators are positioned on the exterior faces of the tensegrity, providing ample internal space for the robot to deform and roll when the actuating-faces inflate (Fig. 4d, Supplementary Movie 10).

We have shown that STAUD-prepreg is a versatile material capable of transforming entirely-soft bodies and hybrid soft-rigid architectures into customized, programmable, and re-configurable deforming systems. The effect of adhered patches on inflating soft bodies is easy to predict due to the simple strain-limiting behavior of the embedded unidirectional fibers. We verified that the shape change of actuators outfitted with STAUD-prepreg is analytically predictable using ACLT, and utilized numerical modeling in ABAQUS to predict compounded motion. Ultimately, we demonstrated highly complex, predictable shape change of 2D and 3D soft bodies reminiscent of the fiber-directed motion of a muscular hydrostat. The fundamental mechanisms of localized, reconfigurable strain-limiting fibers presented herein take a step closer to devising soft robot actuation ever more like real-life fiber musculature that can modulate directional contractions in situ. We expect STAUD-prepreg to become an essential component for controlling synthetic all-soft bodies, but also foresee its adoption into sports, medicine, and rehabilitation spaces due to its ease of implementation and manufacture.

Methods

Materials. To create an elastomer matrix for the lamina, elastomeric platinum-cure resin (Ecoflex 00–30, Smooth-On) was mixed in a 1:1 ratio by weight. The mixture was subjected to 2000 rpm for 1 min in a planetary mixer (Thinky ARE-310) and degassed at 2200 rpm for an additional minute. The pneumatic cylinders, planar actuators, and membrane actuators used in the demonstrations were also fabricated from this resin, to create soft base bladders sufficiently compatible for the STUAD-prepreg to remain adhered. Polyester continuous fibers (100% Spun Thread, PRC) were used as received. The resin for the self-adhesive backing of the lamina was created by mixing a 1:1 weight ratio of silicone adhesive constituent (Silbione 4717, Elkem Silicones). Tabs for uniaxial tension tests were made from muslin fabric (Product #: 8808K11, McMaster Carr) infused with a platinum-cure resin (Dragon Skin 10, SmoothOn).

Prepreg fabrication. We built a fiber-winding machine to fabricate STAUD-prepreg with tunable properties in a scalable fashion. The fiber winder consists of a spool holster, a linearly-translating fiber distributor, a rotating winding mandrel, and controlled via an Arduino with an attached Adafruit V2 motor shield. To create bulk lamina, we entered the desired fiber spacing into the Arduino code. We then secured the polyester fiber spool into its holster adjacent to the fiber-winding machine. Next, the machine automatically wound polyester fibers onto the rotating drum. Subsequently, the elastomer resin was poured onto the fibers and smoothed with a resin scraper to disperse it evenly. We allowed the drum to keep rotating for 12 h to allow the resin to disperse evenly as it cured. A self-adhesive layer was then created on the back of the fully-cured prepreg by applying silicone adhesive that cures at room condition for 12 h. This self-adhesive layer was previously reported to maintain its adhesive force up to 20 attachment/detachment cycles, depending on the preparation of target surfaces[39]. We note that sufficient areal coverage between the adhesive layer and an inflatable body is required for robust attachment. For example, in Fig. 3b the adhesion of the STUAD-prepreg to a cylindrical actuator to induce bending motion was reliable with areal coverage >16%.

Augmented classical laminate theory. We constructed a simplified compliance matrix in the fashion that considers both geometric non-linearity and material non-linearity of fiber-reinforced elastomers (Supplementary Eq. 12). Furthermore, in line with the original classical laminate theory, we account for the angle of fibers of each lamina in a laminate by subjecting them to a transformation matrix (Supplementary Eq. 13). Lastly, we consider the effect of cyclic strain relaxation of STAUD-prepreg via a ratio of regression equations gathered from cycled and un-cycled STAUD-prepreg stress-strain curves. The final formulation of ACLT is written as:

$$\sum_{k=1}^{n} \int_{z_{k-1}}^{z_k} [\mathbf{e}]_{x,y}^{k} \mathrm{d}z = \Gamma_c \left[\sum_{k=1}^{n} [\mathbf{S}]_{x,y}^{k}{}^{-1} \right]^{-1} \sum_{k=1}^{n} \int_{z_{k-1}}^{z_k} [\boldsymbol{\sigma}]_{x,y}^{k} \mathrm{d}z \quad (4)$$

Here, $\mathbf{e}$ and $\boldsymbol{\sigma}$ are Eulerian terms referring to the current principal material coordinates, Γ_c is a cycle-depending scaling factor to adjust for strain relaxation, $\mathbf{S}$ is a simplified compliance matrix which relates in-plane stresses to in-plane strains for laminae, all for an n layered-laminate, where each layer k has thickness

$z_k - z_{k-1}$ and its mid-plane is a distance z_k. The input to the model is a stress term obtained by converting pressure to stress assuming the cylindrical actuators can be modeled as expanding pressure vessels. This model is also supplemented by geometrical boundary conditions outlined in the supplemental document. Results in Figs. 2a and 3a show good agreement between experimentally observed and analytically predicted deformation of the various lamina-wrapped cylindrical actuators.

Finite element analysis. We performed finite element analysis (FEA) simulations using Abaqus (SIMULIA, Providence RI) commercial software in order to fully resolve the strain and stress distributions of each laminae and further account for boundary effects in the various cylindrically shaped actuators. FEA simulations allowed us to predict the deformation of more complex geometrical layouts and localized patches of STAUD-prepreg, and to subsequently replicate these simulated movements and designs in real-life systems (Fig. 3d; Supplementary Movie 7). All simulated models were generated using shell elements using the composite shell section formulation that enables numerical integration of composite shells consisting of several laminae in various orientations. Each STAUD-prepreg lamina was modeled as an anisotropic continuum 3D shell whose constitutive behavior is governed by the Holzapfel-Gasser-Ogden (HGO) anisotropic hyper-elastic continuum model.

Data availability

The data in support of the findings and detailing the studies are available from the corresponding author upon request.

References

1. Kim, D.-H., Ghaffari, R., Lu, N. & Rogers, J. A. Flexible and stretchable electronics for biointegrated devices. *Annu. Rev. Biomed. Eng.* **14**, 113–128 (2012).
2. Tybrandt, K. et al. High-density stretchable electrode grids for chronic neural recording. *Adv. Mater.* **30**, 1706520 (2018).
3. Rogers, J. A., Someya, T. & Huang, Y. Materials and mechanics for stretchable electronics. *Science* **327**, 1603–1607 (2010).
4. Amjadi, M., Kyung, K.-U., Park, I. & Sitti, M. Stretchable, skin-mountable, and wearable strain sensors and their potential applications: a review. *Adv. Funct. Mater.* **26**, 1678–1698 (2016).
5. Wang, S. et al. Skin electronics from scalable fabrication of an intrinsically stretchable transistor array. *Nature* **555**, 83–88 (2018).
6. Choi, W. et al. Multigait soft robot. *Proc. Natl Acad. Sci. USA* **108**, 20400–20403 (2011).
7. Ilievski, F., Mazzeo, A. D., Shepherd, R. F., Chen, X. & Whitesides, G. M. Soft robotics for chemists. *Angew. Chem.* **123**, 1930–1935 (2011).
8. Ranzani, T., Russo, S., Bartlett, N. W., Wehner, M. & Wood, R. J. Increasing the dimensionality of soft microstructures through injection-induced self-folding. *Adv. Mater.* **30**, 1802739 (2018).
9. Majidi, C. Soft robotics: a perspective—current trends and prospects for the future. *Soft Robot.* **1**, 5–11 (2014).
10. Bauer, S. et al. 25th anniversary article: a soft future: from robots and sensor skin to energy harvesters. *Adv. Mater.* **26**, 149–162 (2014).
11. Rus, D. & Tolley, M. T. Design, fabrication and control of soft robots. *Nature* **521**, 467–475 (2015).
12. Laschi, C., Mazzolai, B. & Cianchetti, M. Soft robotics: technologies and systems pushing the boundaries of robot abilities. *Sci. Robot.* **1**, eaah3690 (2016).
13. Gorissen, B. et al. Elastic inflatable actuators for soft robotic applications. *Adv. Mater.* **29**, 1604977 (2017).
14. Martinez, R. V. et al. Robotic tentacles with three-dimensional mobility based on flexible elastomers. *Adv. Mater.* **25**, 205–212 (2013).
15. Wehner, M. et al. An integrated design and fabrication strategy for entirely soft, autonomous robots. *Nature* **536**, 451–455 (2016).
16. Sydney Gladman, A., Matsumoto, E. A., Nuzzo, R. G., Mahadevan, L. & Lewis, J. A. Biomimetic 4D printing. *Nat. Mater.* **15**, 413–418 (2016).
17. Pikul, J. H. et al. Stretchable surfaces with programmable 3D texture morphing for synthetic camouflaging skins. *Science* **358**, 210–214 (2017).
18. Belding, L. et al. Slit tubes for semisoft pneumatic actuators. *Adv. Mater.* **30**, 1704446 (2018).
19. Cappello, L. et al. Exploiting textile mechanical anisotropy for fabric-based pneumatic actuators. *Soft Robot.* **5**, 662–674 (2018).
20. Siéfert, E., Reyssat, E., Bico, J. & Roman, B. Bio-inspired pneumatic shape-morphing elastomers. *Nat. Mater.* **18**, 24–28 (2019).

21. Chou, Ching-Ping & Hannaford, B. Measurement and modeling of McKibben pneumatic artificial muscles. *IEEE Trans. Robot. Autom.* **12**, 90–102 (1996).
22. Tondu, B. & Lopez, P. Modeling and control of McKibben artificial muscle robot actuators. *IEEE Control Syst.* **20**, 15–38 (2000).
23. Martinez, R. V., Fish, C. R., Chen, X. & Whitesides, G. M. Elastomeric origami: Programmable paper-elastomer composites as pneumatic actuators. *Adv. Funct. Mater.* **22**, 1376–1384 (2012).
24. Tolley, M. T. et al. A resilient, untethered soft robot. *Soft Robot.* **1**, 213–223 (2014).
25. Paik, J. Soft robot design methodology for 'push-button' manufacturing. *Nat. Rev. Mater.* **3**, 81–83 (2018).
26. Deimel, R. & Brock, O. A novel type of compliant and underactuated robotic hand for dexterous grasping. *Int. J. Rob. Res.* **35**, 161–185 (2016).
27. Connolly, F., Walsh, C. J. & Bertoldi, K. Automatic design of fiber-reinforced soft actuators for trajectory matching. *Proc. Natl Acad. Sci. USA* **114**, 51–56 (2016).
28. Kurumaya, S. et al. A modular soft robotic wrist for underwater manipulation. *Soft Robot.* **5**, 399–409 (2018).
29. Rafsanjani, A., Zhang, Y., Liu, B., Rubinstein, S. M. & Bertoldi, K. Kirigami skins make a simple soft actuator crawl. *Sci. Robot* **3**, eaar7555 (2018).
30. Kier, W. M. & Smith, K. K. Tongues, tentacles and trunks: the biomechanics of movement in muscular-hydrostats. *Zool. J. Linn. Soc.* **83**, 307–324 (1985).
31. Kier, W. M., Woledge, R. C. & Bone, Q. The diversity of hydrostatic skeletons. *J. Exp. Biol.* **215**, 1247–1257 (2012).
32. Stavness, I., Lloyd, J. E. & Fels, S. Automatic prediction of tongue muscle activations using a finite element model. *J. Biomech.* **45**, 2841–2848 (2012).
33. Kim, S. Y., Jones, A. R., Sottos, N. R. & White, S. R. Manufacturing of unidirectional glass/epoxy prepreg with microencapsulated liquid healing agents. *Compos. Sci. Technol.* **153**, 190–197 (2017).
34. Affdl, J. C. H. & Kardos, J. L. The Halpin-Tsai equations: a review. *Polym. Eng. Sci.* **16**, 344–352 (1976).
35. Hahn, H. T. & Tsai, S. W. Nonlinear elastic behavior of unidirectional composite laminae. *J. Compos. Mater.* **7**, 102–118 (1973).
36. Hahn, H. T. Nonlinear behavior of laminated composites. *J. Compos. Mater.* **7**, 257–271 (1973).
37. Reddy, J. N. A generalization of two-dimensional theories of laminated composite plates. *Commun. Appl. Numer. Methods* **3**, 173–180 (1987).
38. Daniel, I. M. & Ishai, O. Engineering mechanics of composite materials. book (Oxford university press, Oxford, 2006). https://doi.org/10.1016/B978-0-08-006421-5.50049-6
39. Liu, L. et al. Silicone-based adhesives for long-term skin application: cleaning protocols and their effect on peel strength. *Biomed. Phys. Eng. Express* **4**, 015004 (2017).

Author contributions

S.Y.K. and R.K.B. conceived the idea. S.Y.K. and R.B. performed the manufacturing. R.B. and N.V. performed the material characterization and modeling. S.Y.K., R.B. and J.B. performed the demonstrations. K.B. and R.K.B. reviewed and commented on the manuscript. All authors participated in writing the manuscript.

Additional information

Supplementary Information accompanies this paper at https://doi.org/10.1038/s41467-019-11294-7.

Competing interests: The authors declare no competing interests.

Reprints and permission information is available online at http://npg.nature.com/reprintsandpermissions/

Peer review information: *Nature Communications* thanks the anonymous reviewers for their contribution to the peer review of this work. Peer reviewer reports are available.

Publisher's note: Springer Nature remains neutral with regard to jurisdictional claims in published maps and institutional affiliations.

Supplementary Information

Reconfigurable soft body trajectories using unidirectionally stretchable composite laminae

Sang Yup Kim[1†], Robert Baines[1†], Joran Booth[1], Nikolaos Vasios[2], Katia Bertoldi[2,3], Rebecca Kramer-Bottiglio[1*]

[1]Mechanical Engineering and Material Science, School of Engineering and Applied Science, Yale University, 9 Hillhouse Ave, New Haven, CT 06511, USA.

[2]School of Engineering and Applied Sciences, Harvard University, Cambridge, MA 02138, USA.

[3]Kavli Institute, Harvard University, Cambridge, MA 02138, USA.

Correspondence to: rebecca.kramer@yale.edu

Contents

Supplementary Movies

Movie 1: Strain-limiting behavior of STAUD-prepreg

Movie 2: Contraction of pneumatic cylinder

Movie 3: Elongation of pneumatic cylinder

Movie 4: Rotation of pneumatic cylinder

Movie 5: Thin planar actuator bending

Movie 6: Bending of pneumatic cylinder

Movie 7: Octopus-like tentacle movement with localized patches

Movie 8: Planar octopus-inspired actuator

Movie 9: Balloon trajectory programming

Movie 10: Membrane-actuated tensegrity

<u>Supplementary Methods</u>

We built a fiber-winding machine to fabricate STAUD-prepreg with tunable properties in a scalable fashion. The fiber winder consists of a spool holster, a linearly-translating fiber distributor, a rotating winding mandrel. The fiber distributor was prepared using a ball screw (Model #: MTF06011, THK) attached to a stepper motor (Product #: 324, Adafruit) and a metal eye through which the fiber travels. The winding mandrel is an aluminum drum of 175 mm (ϕ) × 225 mm (h) attached to another stepper motor. The metal eye holds the fiber in constant tension as it spools from its holster onto the drum. Both motors are controlled via an Arduino with an attached Adafruit V2 motor shield. Precise inter-fiber spacing of composite lamina is accomplished by varying the rotation rate of the shaft and drum relative to one another.

To conduct uniaxial pull-to-failure tension tests, we fabricated rectangular laminae samples with three distinct inter-fiber spacings, ($\ell = 1$, 2, and 6 mm), as well as three fiber angles, ($\theta = 0°$, 45°, and 90°), by laser-cutting the bulk laminae into discrete units (VLS 3.50, Universal Laser Systems). 12.7 mm-long tabs served as grip interfaces on the samples. The width of the tabs on a particular sample matched the sample's width w. Lengths, L (the distance between the tabs), across all angle/spacing combinations remained fixed at 101.6 mm. Sample widths for the $\theta = 45°$ and $\theta = 0°$ cases were 12.7 mm, but for $\theta = 90°$, was 25.4 mm. Sample average thicknesses, t, were individually characterized using a Zeiss Smartzoom 5 digital microscope. Later, we consider individual thicknesses to calculate stress-strain curves for each sample.

We performed unidirectional quasi-static tensile tests using a servo-hydraulic test machine (Model 3345, Instron). We considered a total of forty-five samples—five of each fiber orientation/spacing combination—to account for inter-sample variance. Pneumatic grips set to 40 psi provided sufficient force to hold 0° samples without allowing slip. Standard set-screw grippers were used for the 90° and 45° samples. We marked test samples with equidistant fiducials (Product#: 846, MG chemicals) about the midpoint of their longitudinal axes, and extracted true strains by tracking the fiducials in high-definition camera footage taken during each trial. For the 90° and 45° lamina, uniaxial tensile loading was applied at 50 mm/min until failure. In the 0° case, we slowed the loading speed to 25 mm/min.

Stress is found by dividing the pull force by the cross-sectional area of the midpoint of the sample:

$$\sigma = \frac{F}{A} \tag{1}$$

To account for changing cross sectional area of the samples we apply a differential form of Poisson's law.

$$A = tw\left(1 - 2\delta + \delta^2\right)$$
$$\delta = 1 - \left(1 + \frac{\Delta L}{L}\right)^{-\upsilon} \tag{2}$$

3

Here, d is the induced contraction normal to the direction of applied strain. Thus, we calculate true stress and observe true strain.

Experimental stress strain curves are summarized in Supplementary Figure 1c, and expanded in more detail in Fig. 2a of the main manuscript. Initial Young's moduli for lamina principal directions 1 and 2, as well shear direction 6 (Supplementary Figure 1), were calculated via averaged linear fit of sample the stress-strain curves from 0.02-0.03 strain (linear region). Off-axis tensile testing of a $\theta = 45°$ sample, as recommended in previous work [1], allowed us to determine the shear modulus of the lamina. Applying a rotation to the tensile stress, σ_x, to transform it about the material axes and obtain laminate coordinate shear stress is simply:

$$\sigma_6 = -\sigma_x \sin\theta \cos\theta \tag{3}$$

where $\theta = -45°$. We acquired shear modulus, G_6, in a similar fashion as the principal lamina moduli, but instead of purely longitudinal strain, we considered the difference between longitudinal and transverse strain (which is in-plane shear strain for 45° off-axis case) [2]. We compare experimentally calculated moduli to theoretical moduli arising from the rule of mixtures (4) and inverse rule of mixtures (5), (6), respectively [2]. We assume the fibers and matrix are each isotropic.

$$E_1 = V_f E_f + V_m E_m \tag{4}$$

$$\frac{1}{E_2} = \frac{V_f}{E_f} + \frac{V_m}{E_m} \tag{5}$$

$$\frac{1}{G_6} = \frac{V_f}{G_f} + \frac{V_m}{G_m} \tag{6}$$

Here, E_1 and E_2 are the elastic moduli of the composite in the 1 or 2 lamina coordinate system directions, respectively, E_f is the elastic modulus of the fibers, G_f is the shear modulus of the fibers, E_m is the elastic modulus of the matrix, G_m is the shear modulus of the matrix, V_m is the volume fraction of the matrix, and V_f is the volume fraction of fibers. We used 68 kPa for the elastic modulus of the matrix material. This value was as determined through tensile tests of a pure Ecoflex 030 sample.

Spun polyester yarn fiber has a range of reported elastic moduli depending on degree of twist [3], tensile conditions during integration to another structure (in our case, spooling on drum for composite manufacture) [4], and a host of other factors, including temperature and humidity [5]. In fact, twisting of individual filaments into bundle can decrease Young's modulus by nearly 33 % [5]. We opted to use a modulus of 1.3 GPa, as discerned from previous work [6]. Following the assumption of fiber isotropy, the shear modulus for the polyester fibers was assumed to be 1.3

GPa as well. The shear modulus of Ecoflex 030, by assuming incompressibility and evoking the isotropic material relation is given as:

$$G = \frac{E}{2(1+\upsilon)} \tag{7}$$

was found to be 22 kPa. This shear modulus is consistent with previously reported values [7].

Theoretically and experimentally calculated initial elastic moduli lie in Supplementary Table S1. From the table, it is clear that a larger volume fraction of fibers, corresponding to a smaller inter-fiber spacing, ℓ, make a lamina stiffer. We see this trend for both 1 and 2 material axes. Expectantly, E_1 is greater than E_2, because the fibers dominate laminae mechanical responses at $\theta = 0°$.

The rule of mixtures tends to overestimate elastic modulus, as it does not take into account micro-voids and geometrical imperfections present in real material samples. This fact helps explain why theoretical elastic moduli values are for the most part above the experimental ones reported above. Imperfect sample alignment during testing could have also contributed to the discrepancy between experimental and theoretical values. The mechanical properties of highly anisotropic composites are very sensitive to fiber alignment, and slightly offset angles can impact behavior substantially [5]. Perhaps this is why we see higher experimental in-plane shear moduli.

Laminae lengths and widths are much greater than their respective thicknesses, so we abide by the assumption posited for in-plane stress-strain relations for thin laminae. Traditionally, the stiffness or compliance matrix constructed for laminae uses fixed moduli and consequently is a linear mapping between strain and stress [2]. We account for the non-linear material behavior of the lamina under plane stress, in addition to the geometric non-linearity of the lamina in its deformed state through a moving Eulerian coordinate system in the fashion of Chou [5], based on work by Hahn and Tsai [8]. Neglecting shear-coupling terms to simplify the expression, the stress-energy per unit area of a deformed lamina can be written as:

$$\begin{aligned}
W^* = & \frac{1}{2}S_{11}\sigma_1^2 + \frac{1}{3}S_{111}\sigma_1^3 + \frac{1}{4}S_{1111}\sigma_1^4 + \\
& S_{12}\sigma_1\sigma_2 + \frac{1}{2}S_{22}\sigma_2^2 + \frac{1}{3}S_{222}\sigma_2^3 + \frac{1}{4}S_{2222}\sigma_2^4 + \\
& \frac{1}{2}S_{66}\sigma_6^2 + \frac{1}{4}S_{6666}\sigma_6^4
\end{aligned} \tag{8}$$

Here, S_{ij}, S_{ijk}, and S_{ijkl} are compliance terms. Chou constructs the simplified compliance matrix following the derivative of the complementary strain energy function

$$\delta W^* = e_{ij}\delta\sigma_{ij} \tag{9}$$

To obtain:

$$e_1 = S_{11}\sigma_1 + S_{111}\sigma_1^2 + S_{1111}\sigma_1^3 + S_{12}\sigma_2$$
$$e_2 = S_{22}\sigma_2 + S_{222}\sigma_2^2 + S_{2222}\sigma_1^3 + S_{12}\sigma_1 \qquad (10)$$
$$e_6 = S_{66}\sigma_6 + S_{6666}\sigma_6^3$$

Note the e and σ are Eulerian terms referring to the current principal material coordinates. We can relate engineering strain ε to Eulerian strain e with the following relation [9]:

$$\varepsilon = \left(\frac{1}{1-2e}\right)^{-1/2} - 1 \qquad (11)$$

The simplified compliance matrix which relates in-plane stresses to in-plane strains along the principal material axes 1 and 2 and shear direction 6 is constructed as such:

$$\mathbf{S} = \begin{bmatrix} S_{11} + S_{111}\sigma_1 + S_{1111}\sigma_1^2 & S_{12} & 0 \\ S_{12} & S_{22} + S_{222}\sigma_2 + S_{2222}\sigma_1^2 & 0 \\ 0 & 0 & S_{66} + S_{6666}\sigma_6^2 \end{bmatrix} \qquad (12)$$

Constants S_{11}, S_{22}, S_{12}, and S_{66} equal $\frac{1}{E_1}$, $\frac{1}{E_2}$, $\frac{-\upsilon_{12}}{E_1}$, and $\frac{1}{G_6}$, respectively, and were obtained based on initial experimental moduli tabulated in Supplementary Table S1. Higher order terms S_{ijk} and S_{ijkl} were determined by fitting experimental stress strain curves according to steps outlined in previous work [5]. MATLAB least squares functions were used for the fitting. Off-axis laminae may be rotated about principal axes to a local loading orientation θ by applying a transformation matrix.

$$\mathbf{T} = \begin{bmatrix} \cos^2\theta & \sin^2\theta & -2\sin\theta\cos\theta \\ \sin^2\theta & \cos^2\theta & 2\sin\theta\cos\theta \\ -2\sin\theta\cos\theta & 2\sin\theta\cos\theta & \cos^2\theta - \sin^2\theta \end{bmatrix} \qquad (13)$$

The stress-strain relations for a lamina can now be written as:

$$[\mathbf{e}] = [\mathbf{T}]^{-1}[\mathbf{S}][\mathbf{T}][\mathbf{\sigma}] \qquad (14)$$

To account for strain relaxation of elastomers as a result of cyclic loading, also known as the Mullins effect [10], we adjust predicted strains arising from our analytical model. A polynomial damage function was constructed based on the stress-strain behavior of the fibrous composite that was un-stretched, and then stretched up to 70% strain 10 times in succession. Tests were conducted up to 20 cycles, and it was determined that there is negligible ($< 5\,\%$) stress-strain change after the 10 cycles threshold. This finding is consistent with other work [10-12]. The damage function relates an un-stretched strain to a cycled strain at the same stress value. We chose G_c to be a cycle-depending scaling factor such that for cycle c:

$$\Gamma_c = \begin{cases} 1 & \text{if} \quad c = 1 \\ \dfrac{\beta_0 + \beta_1\sigma + \beta_1\sigma^2 + \beta_1\sigma^3}{\beta_0' + \beta_1'\sigma + \beta_1'\sigma^2 + \beta_1'\sigma^3} & \text{if} \quad c > 1 \end{cases} \tag{15}$$

Here, b_i are coefficients for the third-order polynomial fit of the average un-cycled curve, while b_i' are those for the average cycled curve. We can write our final formulation for predicting lamina strain as a function of input stress and cycle number:

$$[\mathbf{e}] = \Gamma_c [\mathbf{T}]^{-1}[\mathbf{S}][\mathbf{T}][\boldsymbol{\sigma}] \tag{16}$$

For n layered-laminate, where each layer k has thickness $z_k - z_{k-1}$ and its mid-plane is a distance z_k from the mid-plane of the total laminate [2]:

$$\sum_{k=1}^{n} \int_{z_{k-1}}^{z_k} [\boldsymbol{\sigma}]_{x,y}^{k} \, dz = \sum_{k=1}^{n} \int_{z_{k-1}}^{z_k} [\mathbf{Q}]_{x,y}^{k} [\boldsymbol{\varepsilon}]_{x,y}^{k} \, dz \tag{17}$$

Q is the stiffness matrix. As we are interested in the continuous strains through the thickness of the laminate, we must consider the inversion of the above relation. Note that:

$$[\mathbf{Q}] = [\mathbf{S}]^{-1} \tag{18}$$

Having accounted for material non-linearity (not present in assumptions in classical laminate theory) according to third order polynomial modeling based off the complementary stress energy density function, geometric non linearity with an Eulerian coordinate system, as well as cyclic stress-strain behavior of our matrix material with a Mullins damage function, we can model the creation of STAUD-prepreg laminates. We dub this adaptation Augmented Classical laminate theory (ACLT). We express it mathematically as:

$$\sum_{k=1}^{n} \int_{z_{k-1}}^{z_k} [\mathbf{e}]_{x,y}^{k} \, dz = \Gamma_c \left[\sum_{k=1}^{n} [\mathbf{S}]_{x,y}^{k\,-1} \right]^{-1} \sum_{k=1}^{n} \int_{z_{k-1}}^{z_k} [\boldsymbol{\sigma}]_{x,y}^{k} \, dz \tag{19}$$

Using our adapted formulation of classical laminate theory, we predicted the engineering strain of cylindrical actuators as a function of applied input stress. We conducted tests on three baseline cases of actuators (n = 1): 90°, 0°, and 45° fiber orientation. We also explored creation of laminate actuators (n = 2): 90°+0° and 90°+45°. We cycled the cylinders 10 times before conducting each test, breaking them in to a repeatable range. We adjusted analytical results with the strain relaxation damage function detailed above. We acquired stress by transforming input pressure read from a pressure sensor (Model#: 015PGAA5, Honeywell) using thin-walled pressure vessel equations.

Our model assumes gravitational forces acting on the cylinder are negligible. We ignore inter-layer adhesive layer thicknesses as well. We model an inflating pneumatic cylinder as a thin

wall pressure vessel (Supplementary Figure 2) because its wall thickness is much smaller than its radius [13]. Circumferential hoop and axial stresses are the only forces acting on a thin-walled pressure vessel and are purely planar forces that give a mapping between applied pressure and stresses experienced in the laminate coordinates.

$$\sigma_{axial} = \frac{pr}{2t}$$

$$\sigma_{hoop} = \frac{pr}{t}$$

(20)

where p is the known input pressure, r is the radius of the cylinder, and t is the thickness of the wall.

In the 0° cylindrical actuator case, inflation causes transverse expansion, which subsequently induces contraction as fibers pull the bottom of the actuator up. We modeled the fiber deformation to have constant curvature, and applied the geometrical constraints detailed in Supplementary Figure 3 to calculate theoretical contraction based on theoretical transverse strain. In Supplementary Figure 3, l is the resulting length of the cylinder after it has contracted some distance Δl from an original length l_0. The induced arc of deformation is approximated by a secant line of length $\frac{l_0}{2}$, as pictured. The instantaneous radius, r, is updated based on the theoretical transverse strain: $r = \varepsilon r_0 + r_0$. Note the relation depicted by Supplementary Figure 3 holds only when

$$\frac{l_0}{2} > (r - r_0)$$

(21)

Finally, we must consider the thickness change of the vessel walls as a function of expansion to get an accurate representation of the stress states. In line with our planar stress assumption, out-of-plane stresses are not considered, and we can express the instantaneous thickness of the pneumatic actuator as

$$t = t_0 \varepsilon_z + t_0$$

(22)

Since

$$\varepsilon_z = -\upsilon \varepsilon_x - \upsilon \varepsilon_y$$

(23)

Fig. 2a and 3a in the main manuscript show good agreement between experimentally observed and analytically predicted deformation of the various lamina-wrapped cylindrical actuators. For the 0° case, the model reliably predicts up to a certain value of strain, usually around 20 %, after which geometric effects not considered by our model, including fiber anchoring to the end caps of the inflating cylinder, begin to govern the stiffness of the system so we see significant deviation. Additional differences between theoretical and experimental strain values may have

arisen since we inflated the cylinders at a greater rate ($\times$ 20) than quasi-static conditions on of which the material moduli were derived. As such, our experimental curves may reflect hyper-viscoelastic effects. Overall, we achieve reliable prediction of deformation of soft bodies clad in sequences of angle-ply laminates in a range of strains suited to soft robotic applications.

In an effort to validate our experimental and analytical findings using ACLT but also to enable the modelling of more complex geometries and multi-layered STAUD-prepeg laminate actuators, we performed finite element analysis (FEA) simulations using Abaqus (SIMULIA, Providence RI) commercial software. FEA allowed us to fully resolve the strain and stress distributions of each laminae and further account for boundary effects in the various cylindrically shaped actuators. All models were generated using shell elements (S4R) using the composite shell section formulation that enables numerical integration of composite shells consisting of several laminae in various orientations. We performed nonlinear quasi-static analyses using Abaqus/Explicit to simulate the deformation of cylindrically shaped actuators upon inflation. To ensure quasi-static conditions in the simulations, we verified that the kinetic energy associated with the finite loading and deformation rate of the actuators was at all times negligible compared to the strain energy in each model. All cylindrically shaped actuators were assumed to have strain-free caps, one of which was held fixed to eliminate rigid body translations and rotations. The actuators were inflated using the fluid-filled cavity interaction, corresponding to volume-controlled loading conditions. Each STAUD-prepreg lamina was modelled as an anisotropic continuum 3D shell whose constitutive behavior is governed by the Holzapfel-Gasser-Ogden (HGO) anisotropic hyper-elastic continuum model [14]. The strain energy density function associated with the HGO model takes the form,

$$\mathcal{W} = C_{10}(I_1 - 3) + \frac{k_1}{2k_2}\left(e^{k_2(I_4-1)^2} - 1\right) \tag{24}$$

where,

$$I_1 = \text{tr}[B] \tag{25}$$

$$I_4 = (F \cdot \mathbf{M}) \cdot (F \cdot \mathbf{M}) \tag{26}$$

and $B = F \cdot F^{\text{T}}$ is the left Cauchy-Green deformation tensor and M is the unit vector along the fiber direction in the reference configuration. The material parameters of the constitutive model, namely C_{10}, k_1, and k_2 are determined by fitting the model to experimental data, preferably containing information for the behavior of the sample in various fiber orientations. Here, we used nominal stress-nominal strain data corresponding to uniaxial extension experiments along 0º, 45º, and 90º orientations, and we performed non-linear least square fits against the corresponding stress-strain expressions for the HGO model. In the following section, we determine the nominal stress-strain relationships for the uniaxial extension of a thin film obeying the HGO model.

The nominal stress tensor can be determined from the strain energy function,

$$S = \frac{\partial \mathcal{W}}{\partial F} = \det F \cdot F^{-1} \cdot \sigma \tag{27}$$

where σ is the Cauchy stress tensor, which from an HGO anisotropic solid takes the form,

$$\sigma = -pI + 2\frac{\partial \mathcal{W}}{\partial I_1}F \cdot F^T + 2\frac{\partial \mathcal{W}}{\partial I_4}m \otimes m \tag{28}$$

where p is a hydrostatic stress and $m = F \cdot M$ is the unit vector along the fiber direction in the current (deformed) configuration. The deformation gradient tensor for an incompressible HGO anisotropic hyper-elastic material subjected to uniaxial extension has the form,

$$F = \lambda_x e_1 e_1 + \lambda e_2 e_2 + \lambda_z e_3 e_3 \tag{29}$$

and incompressibility implies that,

$$\lambda_x = \frac{1}{\lambda \lambda_z} \tag{30}$$

The corresponding left Cauchy-Green deformation tensor $\mathbf{B} = \mathbf{F} \cdot \mathbf{F}^T$ follows,

$$\mathbf{B} = \frac{1}{\lambda^2 \lambda_z^2}e_1 e_1 + \lambda^2 e_2 e_2 + \lambda_z^2 e_3 e_3 \tag{31}$$

Given that the loading (extension) direction is along the e_2 unit vector, we can further define θ as the angle between the fiber direction s and the loading direction. The fiber direction in the reference configuration can thus be expressed as

$$\mathbf{M} = \sin\theta\, e_1 + \cos\theta\, e_2 \tag{32}$$

The fourth pseudo-invariant I_4 of the left Cauchy-Green tensor B is given by,

$$I_4 = (F \cdot \mathbf{M}) \cdot (F \cdot \mathbf{M}) = \lambda^{-2}\lambda_z^{-2}\sin^2\theta + \lambda^2\cos^2\theta \tag{33}$$

Furthermore, we have that,

$$\frac{\partial \mathcal{W}}{\partial I_1} = C_{10}$$

$$\frac{\partial \mathcal{W}}{\partial I_4} = k_1(I_4 - 1)e^{k_2(I_4-1)^2} \tag{34}$$

$$m = F \cdot \mathbf{M} = \lambda^{-1}\lambda_z^{-1}\sin\theta\, e_1 + \lambda\cos\theta\, e_2$$

$$m \otimes m = \lambda^{-2}\lambda_z^{-2}e_1 e_1 + \lambda_z^{-1}\sin\theta\cos\theta\,(e_1 e_2 + e_2 e_1) + \lambda^2\cos^2\theta\, e_2 e_2$$

Therefore, combining the expressions above, the components of the Cauchy stress tensor σ_{ij} may be calculated as follows,

$$\sigma_{11} = -p + 2C_{10}\lambda^{-2}\lambda_z^{-2} + 2k_1\lambda^{-2}\lambda_z^{-2}\sin^2\theta\,(I_4 - 1)e^{k_2(I_4-1)^2}$$

$$\sigma_{12} = 2k_1\lambda_z^{-1}\sin\theta\cos\theta\,(I_4 - 1)\,e^{k_2(I_4-1)^2}$$

$$\sigma_{13} = 0$$

$$\sigma_{21} = 2k_1\lambda_z^{-1}\sin\theta\cos\theta\,(I_4 - 1)\,e^{k_2(I_4-1)^2} \tag{35}$$

$$\sigma_{22} = -p + 2C_{10}\lambda^2 + 2k_1\lambda^2\cos^2\theta\,(I_4 - 1)e^{k_2(I_4-1)^2}$$

$$\sigma_{23} = 0$$

$$\sigma_{31} = 0$$

$$\sigma_{32} = 0$$

$$\sigma_{33} = -p + 2C_{10}\lambda_z^2$$

Finally, the nominal stress tensor components are determined as

$$S_{11} = F_{11}^{-1}\sigma_{11} = -p\lambda\lambda_z + 2C_{10}\lambda^{-1}\lambda_z^{-1} + 2k_1\lambda^{-1}\lambda_z^{-1} \sin^2\theta\,(I_4 - 1)e^{k_2(I_4-1)^2}$$

$$S_{12} = F_{11}^{-1}\sigma_{12} = 2k_1\lambda \sin\theta \cos\theta\,(I_4 - 1)\,e^{k_2(I_4-1)^2}$$

$$S_{13} = F_{11}^{-1}\sigma_{13} = 0$$

$$S_{21} = F_{22}^{-1}\sigma_{21} = 2k_1\lambda^{-1}\lambda_z^{-1} \sin\theta \cos\theta\,(I_4 - 1)\,e^{k_2(I_4-1)^2}$$

$$S_{22} = F_{22}^{-1}\sigma_{22} = -p\lambda^{-1} + 2C_{10}\lambda + 2k_1\lambda \cos^2\theta\,(I_4 - 1)e^{k_2(I_4-1)^2} \qquad (36)$$

$$S_{23} = F_{22}^{-1}\sigma_{23} = 0$$

$$S_{31} = F_{33}^{-1}\sigma_{31} = 0$$

$$S_{32} = F_{33}^{-1}\sigma_{32} = 0$$

$$S_{33} = F_{33}^{-1}\sigma_{33} = -p\lambda_z^{-1} + 2C_{10}\lambda_z$$

Since the sample is extended along e_2, the traction free conditions on faces e_1 and e_3 suggest that

$$S_{11} = 0 \;\Rightarrow\; -p\lambda\lambda_z + 2C_{10}\lambda^{-1}\lambda_z^{-1} + 2k_1\lambda^{-1}\lambda_z^{-1} \sin^2\theta\,(I_4 - 1)e^{k_2(I_4-1)^2} = 0 \qquad (37)$$

$$S_{33} = 0 \;\Rightarrow\; -p\lambda_z^{-1} + 2C_{10}\lambda_z = 0 \;\Rightarrow\; p = 2C_{10}\lambda_z^2 \qquad (38)$$

Combining the last two equations, leads to the following non-linear equation

$$\lambda_z^4 = \lambda^{-2}\left[1 + \frac{k_1}{C_{10}} \sin^2\theta\,(I_4(\lambda_z) - 1)e^{k_2(I_4(\lambda_z)-1)^2}\right] \qquad (39)$$

where

$$I_4(\lambda_z) = \lambda^{-2}\lambda_z^{-2} \sin^2\theta + \lambda^2 \cos^2\theta \qquad (40)$$

The non-linear equation needs to be solved with respect to λ_z for each value of λ. Once λ_z is known, the nominal stress S_{22} along the extension direction can be determined using,

$$S_{22} = 2C_{10}(\lambda - \lambda_z^2\lambda^{-1}) + 2k_1\lambda \cos^2\theta\,(I_4 - 1)e^{k_2(I_4-1)^2} \qquad (41)$$

Having determined an expression for the nominal stress component along the uniaxial extension direction, we fit the analytical expression to experimental data of uniaxial extension of samples at $\theta = 0°, 45°$ and $90°$. We did this for each STAUD-prepreg inter-fiber spacing. The fitted material properties for each inter-fiber spacing are summarized in Supplementary Table S2.

Supplementary References

[1] M.-J. Pindera and C. T. Herakovich, Shear characterization of unidirectional composites with the off-axis tension test. *Experimental Mechanics*, **26**, 103–112 (1986).

[2] I. M. Daniel, O. Ishai, *Engineering mechanics of composite materials* (Oxford university press, New York, ed. 2, 2006).

[3] S. Rajendran, S. Ramasamy, and S. P. Mishra, Tensile behavior of polyester yarns modified by trichloroacetic acid–methylene chloride treatment. *Journal of Applied Polymer Science*, **59**, 99–108 (1996).

[4] V. Midha, A. Mukhopadhyay, R. Chattopadhyay, and V. K. Kothari, Studies on the Changes in Tensile Properties of Sewing Thread at Different Sewing Stages. *Textile Research Journal,* **79**, 1155–1167 (2009).

[5] Chou, T-W., Microstructural Design of Fiber Composites (Cambridge University Press, Cambridge, 1992).

[6] M. Zubair, thesis, Technical University of Liberec (2017).

[7] J. L. Sparks et al., Use of silicone materials to simulate tissue biomechanics as related to deep tissue injury. Adv Skin Wound Care, **28**, 59–68 (2015).

[8] H. T. Hahn, S. W. Tsai, Nonlinear elastic behavior of unidirectional composite laminae. *J. Compos. Mater.,* **7**, 102–118 (1973).

[9] S. Luo and T. Chou. Finite Deformation and Nonlinear Elastic Behavior of Flexible Composites. *Journal of Applied Mechanics*, **55** (1988).

[10] J. Diani, B. Fayolle, and P. Gilormini, A review on the Mullins effect. *European Polymer Journal,* **45** (2009).

[11] J. C. Case, E. L. White, and R. K. Kramer, Soft Material Characterization for Robotic Applications. *Soft Robotics,* **2** (2015).

[12] A. Dorfmann and R.W. Ogden, A constitutive model for the Mullins effect with permanent set in particle-reinforced rubber. *International Journal of Solids and Structures*, **41** (2004).

[13] Roy R. Craig, Jr, *Mechanics of Materials.* (John Wiley & Sons, Hoboken, NJ, ed. 3, 2011).

[14] A. Holzapfel, T. C. Gasser, and R. W. Ogden. A new constitutive framework for arterial wall mechanics, *J Elast.*, **61**:1-48 (2000).
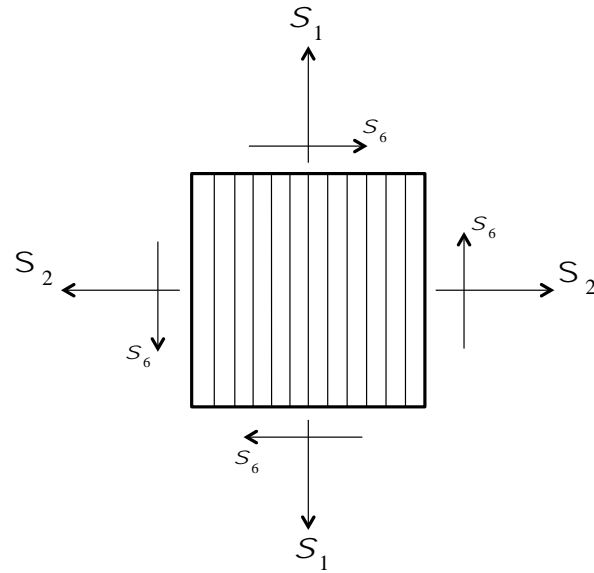
Supplementary Figure 1. Schematic defining lamina principal directions. (1) represents stresses and strains in the direction of embedded fibers, while (2) is transverse to the direction of the fibers. (6) is the in-plane shear component.
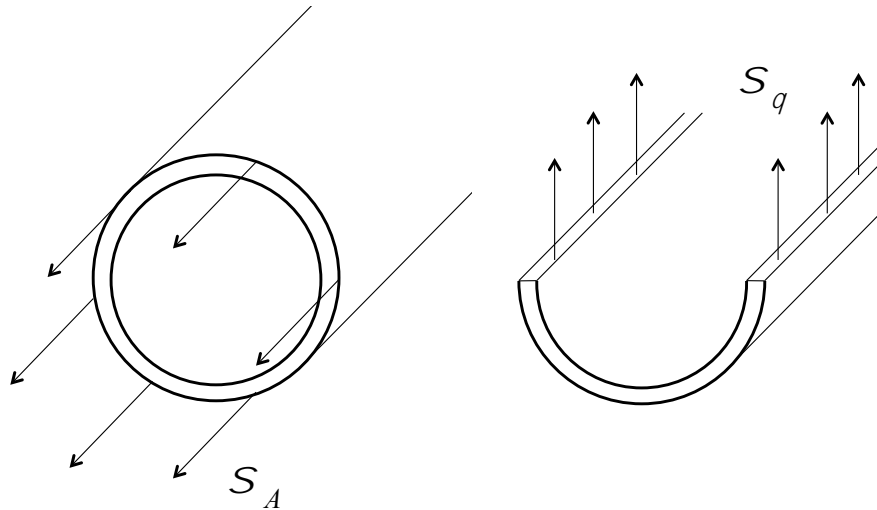

Supplementary Figure 2. Cross section a of thin-wall cylindrical pressure vessel illustrating the distribution of planar stresses. We model our pneumatic actuators under this assumption. Left: tangential hoop stress from cutting the cylinder along its height. Right: axial planar stress observed by cutting the cylinder through its width.

$$l \approx 2\sqrt{\left(\frac{l_0}{2}\right)^2 - \left(r - r_0\right)^2}$$
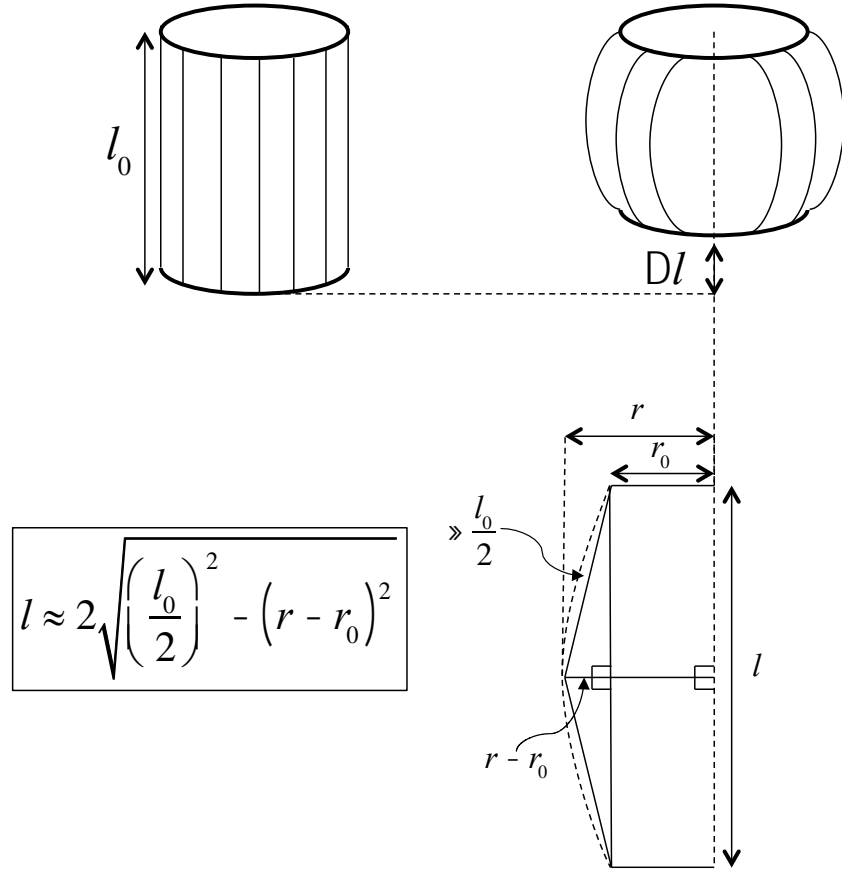
Supplementary Figure 3. Geometric model to account for the contraction of cylindrical pneumatic actuators wrapped with 0° STAUD-prepreg. When inflating, an initial radius r_0 increases to r. Meanwhile, an initial length l_0 shortens by $\mathrm{D}l$ due to fibers "pulling up" the bottom of the cylinder. Approximating the deformed arc as two equivalent right triangles, the induced arc of deformation can be written as $\dfrac{l_0}{2}$ by the Pythagorean theorem.
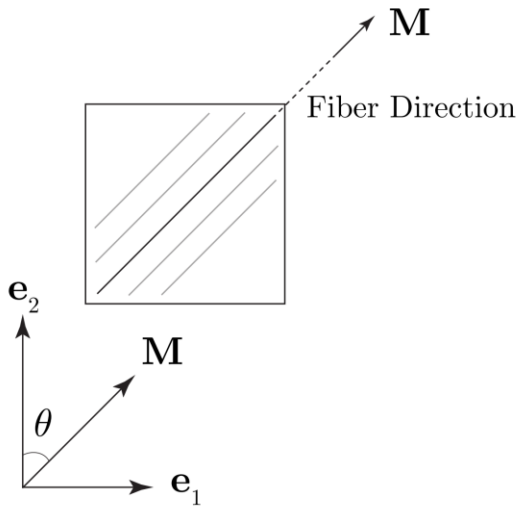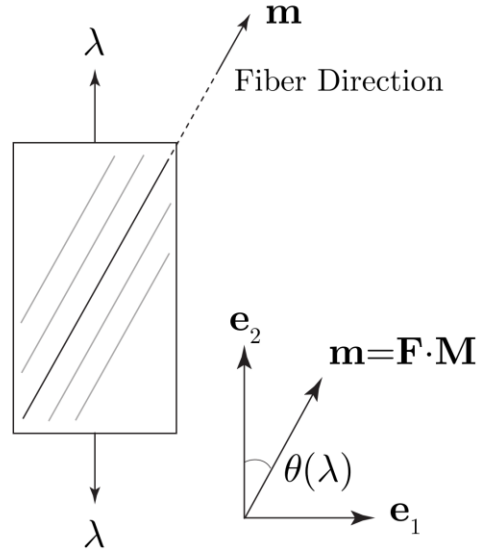
Supplementary Figure 4. Schematic of a fiber-reinforced hyper-elastic material subjected to uniaxial extension. a) **M** is the unit vector along the fiber direction in the reference configuration and θ is the angle between the fiber and loading directions. b) $\boldsymbol{m}$ is the unit vector along the fiber direction in the current configuration after applying a uniaxial stretch equal to λ.
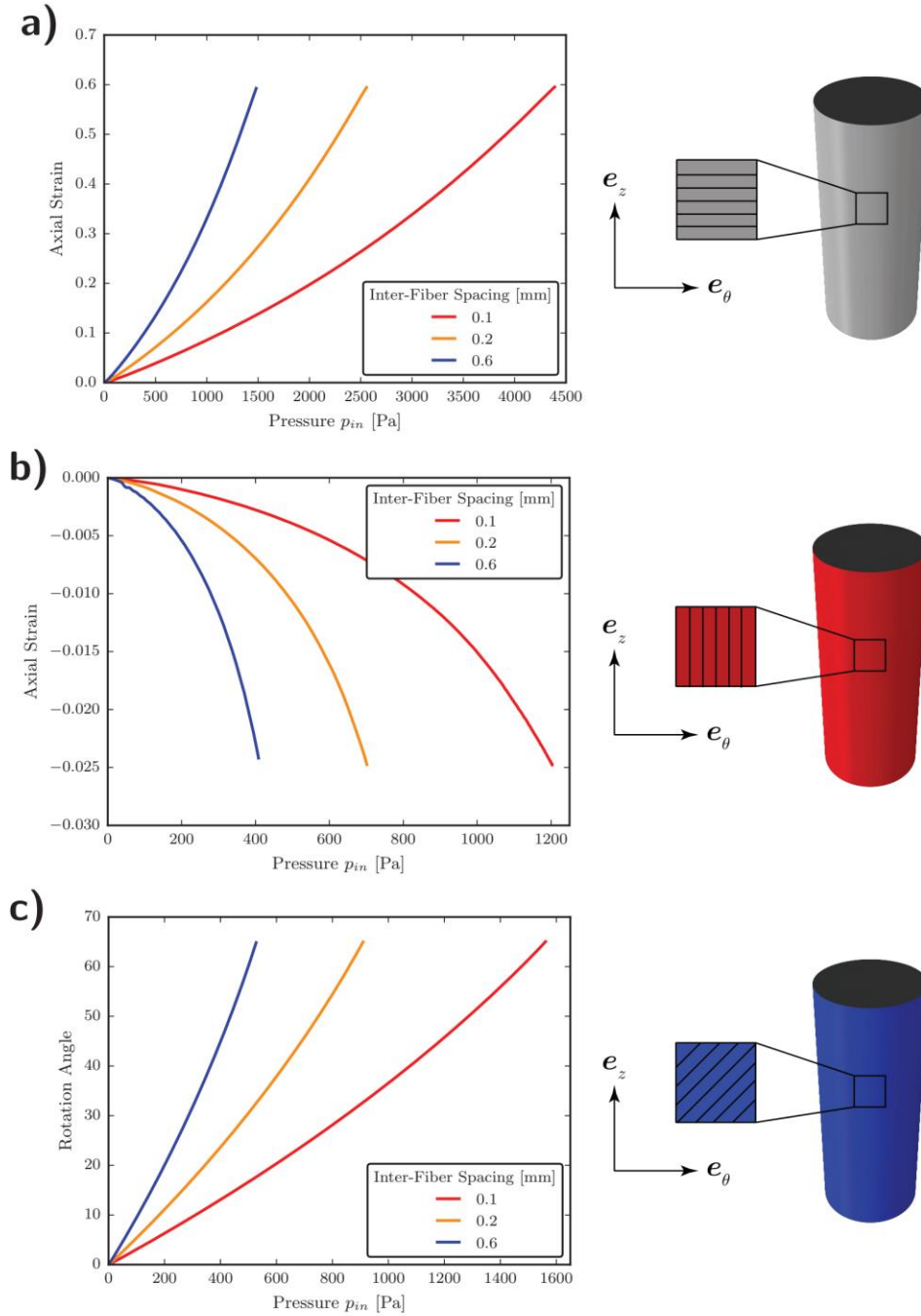
Supplementary Figure 5. FEA results for the quasi-static inflation of cylindrical actuators consisting of a single STAUD-prepreg, with three different inter-fiber spacings, wrapped at three different orientations. a) STAUD-prepreg wrapped at 90° produces an actuator that extends

upon inflation. b) STAUD-prepreg wrapped at 0° elicits an actuator that contracts upon inflation. c) STAUD-prepreg wrapped at 45° creates an actuator that twists upon inflation.

Experimental versus Theoretical Moduli			
Inter-Fiber Spacing [mm]	Directional Moduli	Experimental [MPa]	Rule of Mixtures [MPa]
$\ell = 0.1$	E_1	137	318
	E_2	0.084	0.090
	G_{12}	0.075	0.029
$\ell = 0.2$	E_1	56	159
	E_2	0.070	0.077
	G_{12}	0.048	0.025
$\ell = 0.6$	E_1	22	53
	E_2	0.050	0.070
	G_{12}	0.042	0.023

Supplementary Table 1. Tabulation of collected initial moduli data for the various fiber spacings. Decreasing inter-fiber spacing leads to stiffer laminae. The rule of mixtures tends to overestimate the modulus compared to experimental values.

		Inter-Fiber Spacing mm		
		$l_1 = 0.1$	$l_2 = 0.2$	$l_3 = 0.6$
HGO Fitted Material Parameter	C_{10} [MPa]	0.0204	0.0119	0.006918
	k_1 [MPa]	24.3745	11.797	5.1578
	k_2	2.98e-8	2.1062e-8	2.1062e-8

Supplementary Table 2. Fitted Holzapfel-Gasser-Ogden (HGO) material parameters for the three different inter-fiber spacings. The values were determined through a non-linear least squares fit of the experimental data for the uniaxial extension of each sample along $\boldsymbol{\theta = 0°, 45°}$, and 90°.